Journal of Science: Advanced Materials and Devices 9 (2024) 100642

Contents lists available at ScienceDirect

Journal of Science: Advanced Materials and Devices

journal homepage: www.elsevier.com/locate/jsamd

Improvement of photocatalytic performance and sensitive ultraviolet photodetectors using AC-ZnO/ZC-Ag_2O/AZ-CuO multilayers nanocomposite prepared by spin coating method

Bouras Dikra [a,b], Mamoun Fellah [c,d,**], Regis Barille [e], Sabine Weiß [f], Mohammed Abdul Samad [g], Alhanouf Alburaikan [h], Hamiden Abd El-Wahed khalifa [h,i], Aleksei Obrosov [f,*]

[a] Laboratory of Active Components and Materials (LCAM), University of Larbi Ben M'hidi, 04000, Oum El Bouaghi, Algeria
[b] Faculty of Science and Technology, University of Souk-Ahras, Algeria
[c] Mechanical Engineering Department, ABBES Laghrour- Khenchela University, PO 1252, CP, 40004, Algeria
[d] Research Team, Biomaterial, Synthesis and Tribology, ABBES Laghrour-University, Khenchela, P.O 1252, 40004, Algeria
[e] MOLTECH-Anjou, Universitéd'Angers/UMR CNRS 6200, 2 Bd Lavoisier, 49045, Angers, France
[f] Department of Physical Metallurgy and Materials Technology, Brandenburg Technical University, 03046, Cottbus, Germany
[g] Mechanical Engineering Department & IRC-AM, King Fhad University of Petroleum and Minerals, Dhahran, 31261, Saudi Arabia
[h] Department of Mathematics, College of Science and Arts, Qassim University, Al- Badaya, 51951, Saudi Arabia
[i] Department of Operations and Management Research, Faculty of Graduate Studies of Statistical Research, Cairo University, Giza, 12613, Egypt

ARTICLE INFO

Keywords:
Multilayer CAZO/CZAO/ZACO
Spin-coating
Energy gap
Photocatalysis
Photodetector
Nanostructures
Nanocomposites

ABSTRACT

Morphological and optical properties of a multilayer film (CAZO/CZAO/ZACO) prepared by spin-coating method and deposited on a glass substrate were evaluated. The study was initially carried out for each layer, individually and then as a multilayer subsequently. Structural properties using X-ray diffraction (XRD), energy-dispersive X-ray spectroscopy (EDS), infrared spectra (IR) and X-ray photoelectron Spectroscopy (XPS) showed the presence of three phases of zinc, copper and silver oxides at different levels. The CZAO sample observed with a scanning electron microscope (SEM) showed an excellent porous surface with a large deformation in the multilayer configuration. Doping with zinc and copper in the silver crystal lattice improved the crystal structure and reduced the optical energy gap, thus increasing the optical absorbance and refractive index. The dielectric constants ε_r and ε_i showed an increase in the optical polarization values for lower photonic energies. The maximum degradation rate for photocatalysts of methylene blue was 89 % for a 5-h exposure period with CAZO/CZAO/ZACO while it reached 71 % for the CZAO sample during the same time period. The sensitivity of samples to light proved that the presence of ultraviolet radiation increases the number of holes trapped by oxygen ions and causes more free electrons and contribute to a better production of photocurrent than in darkness.

1. Introduction

Dyes are considered one of the most important pollutants in aquatic systems [1]. The quantity of dyes produced in 1996 reached 4.5 million tons, and most of these quantities are used in industries and in textile industries [2]. Most dyes are either inert or non-toxic [3], but some of them have significant toxic effects on human health and the living environment [4].

The high percentage of organic pollutants in river water as a result of the polluted water being dumped without treatment processes is very dangerous for living organisms in general. Among these pollutants, dyes such as methylene blue (MB) are considered as a low toxic agent and can cause various harmful effects [5,6]. Doses or concentrations more than 7 mg/kg may cause harm to humans by giving rise to health problems such as nausea, abdominal pain and confusion [7,8].

Furthermore, these pigments release nitrates and phosphates in nature [9]. These abundantly released metal ions can become toxic to fish life due to the poisoning of the water [10]. Its consumption by aquatic

Peer review under responsibility of Vietnam National University, Hanoi.
* Corresponding author. Department of Physical Metallurgy and Materials Technology, Brandenburg Technical University, 03046, Cottbus, Germany.
** Corresponding author. Mechanical Engineering Department, ABBES Laghrour- Khenchela University, PO 1252, CP, 40004, Algeria.
E-mail addresses: mamoune.fellah@univ-khenchela.dz (M. Fellah), aleksei.obrosov@b-tu.de (A. Obrosov).

https://doi.org/10.1016/j.jsamd.2023.100642
Received 19 August 2023; Received in revised form 16 October 2023; Accepted 23 October 2023
Available online 30 November 2023

plants accelerates its spread and leads to the depletion of oxygen through the process of photosynthesis in the deepest layers of rivers and stagnant water [11]. Moreover, the accumulation of organic matter in waterways leads to the emergence of bad tastes, the spread of bacteria, unpleasant odors and abnormal colors [12].

The semiconductor research is always in search of materials with good electronic properties [13]. The study of deposited materials in thin layers is one of the best ways to learn about many of their physical and chemical properties, which are difficult to obtain naturally [14]. Transparent carrier oxides are materials used in many electronic applications, such as solar cells, gas sensors, and LEDs.

From previous studies, zinc oxide (ZnO) [15], when bound to metallic copper, has been found to give remarkable results in catalysis [16]. In the quest to achieve better results in this field of research, thin films were prepared based on ZnO (zinc oxide), Ag_2O (silver oxide), and CuO (copper oxide) [17]. The structural, electronic, and optical properties of the surface were studied and compared to other materials [18–21].

For photocatalytic applications, there are several properties that give ZnO advantages over other catalysts [22]. ZnO has much less charge recombination which results in longer lifetimes of charge carriers [23]. The charge transport of ZnO is also very high, at least in crystalline ZnO materials. For particle-based materials, charge transfer is reduced by grain boundaries [24]. In synthesis, solution-based methods are sometimes preferred because they can provide good control over sample shape and crystal growth [25].

A proper bandgap for visible light absorption is a parameter these three oxides have in common. Visible light absorption is also the driver of many studies of these compounds ZnO–CuO–AgO. There are several promising results for the use of CuO as photocatalysts [26,27]. Previous studies based on plasmatic silver nanostructures [28] or in a mixture of silver-copper alloys have already demonstrated their potential not only for visible broadband NIR photocatalysis, but also for solar harvesting, electrocatalysis, bacteria purification, field emission enhancement or for the formation of new superconducting structures [29].

However, there are also some drawbacks of these compounds such as the formation of electron-hole pairs with very low energy at low band gaps, which could decay some stable compounds, or a high charge recombination resulting in its transfer by lower charge carriers [30,31]. Therefore, the synthesis of a heterogeneous hybrid catalyst combining the plasmonic properties of Ag and the semiconducting capabilities of n-type ZnO and p-type CuO to reduce these defects by simultaneously incorporating the three elements reveal strong potential for large-scale photocatalytic applications, since these materials are abundant and affordable [32].

The aim of the present study is to investigate and compare single thin films with multilayer films consisting of three oxides of zinc, silver, and copper to study the effect of doping on the structural, optical properties [33], photodetector performances and photocatalysis and the corresponding change of properties depending on the type and percentage of doping [34]. Cheap, easy, and simple sol-gel fabrication allows us to prepare high-quality oxide thin films that are comparable to those prepared using the most advanced and expensive equipment [35].

The main objective of this work is to know the most influential element among zinc oxide [36], copper [37] and silver [38] and their addition ratios on the structural and morphological properties of the crystal lattice (the occurrence of deformation) and the nanomaterials formed. A comparison was performed between them from the perspective of photocatalytic applications to identify the most effective of them, and to highlight its ability to remove impurities of the toxic organic dye such as methylene blue [39]. The results showed that the multiple layers (CAZO/CZAO/ZACO) are very positive and faster than the thin layers individually in the solution gradation process in the presence of visible light [40]. This improvement is due to the effective surface area of the multilayers sample and the size of its nanoparticles, as increasing the surface temperature led to an acceleration of the process, polarization, and greater absorption of impurities [41]. Samples are prepared in an easy and inexpensive way, with strong layers placed on glass substrates, which is very positive in the application of photocatalysts, as they are easy to withdraw after the filtration process is completed.

Thin layers have brought about a tremendous revolution in the field of nanotechnology, due to the size of their nanoparticles, which play an important role in several other applications beneficial to humans and the environment. It is used as a material in the electronics industry [42], energy fields [43], solar cells [44], sensors [45], and information storage. Instead of traditional three-dimensional materials, which are expensive to produce compared to thin layers, which provide us with ease of preparation and economy of materials.

2. Experimental

2.1. Materials

Zinc acetate [($Zn(CH_3COO)_2$; 99.5 % purity], copper acetate [($Cu(CH_3COO)_2$; 99.0 % purity], silver nitrate [AgNO3; 99.9 % purity] along with Absolute ethanol (C_2H_5OH; purity 99.9 %) and monoethanolamine (C_2H_7NO; purity 90.0 %) were used. The photocatalytic test was carried out on an aqueous solution of MB ($C_{16}H_{18}ClN_3S$; MB with concentration of 4 mg/l). Glass slides with an area of 25.4 × 76.2 mm and a thickness of 1–1.2 mm were used as substrates for depositing the films.

2.1.1. Thin layers deposition

Three solutions were prepared:

Solution 1: Cu–Ag co-doped with ZnO (CAZO). Zinc oxide was chosen as a substrate doped with silver (25 %) and copper (25 %). A 0.4 M concentrated zinc acetate, copper acetate and silver nitrate were added to absolute ethanol solvent, along with MEA catalyst in a molar ratio of 1:1. The solution was then placed on a magnetic stirrer at 70 °C for an hour. The same process was done when preparing the other solutions by changing the base element and maintaining the same doping percentage.

Solution 2: Cu–Zn co-doped AgO (CZAO).

Solution 3: Zn–Ag co-doped CuO (ZACO).

The sol-gel process involves the mixing of liquid precursors which are transformed into a solid by a chemical reaction of polymerization at a low temperature. The most commonly used technique for sol-gel preparation is “spin-coating” [46]. The prepared solution was deposited on a glass substrate at room temperature with a rotational speed of 3000 rpm for 30 s. After sedimentation of each layer, the sample was removed from the apparatus and placed in a drying oven at 250 °C for 10 min. The process was repeated three times for obtaining the CAZO, CZAO and ZACO layers.

The CAZO/CZAO/ZACO sample is multi-layered. The first layer was spin-coated with the solution of CAZO, followed by deposition of the second layer with the solution of CZAO, and then the last layer was deposited with the solution of ZACO, while maintaining the same rotational speed and time (Fig. 1).

2.2. Characterization techniques

The crystal structure of the samples was determined by X-ray diffraction (Bruker AXS-D8) using a Cu Kα radiation (λ = 1.5406 Å). The scanning parameters were set as follows: voltage = 40 kV, current = 30 mA, goniometer angle 2θ = 30°–60°, step size = 0.02°, scan speed = 0.5 s/step and divergence slit = 0.6 mm.

A scanning electron microscope (JSM-6301F) was used to study the morphology of the samples. The infrared spectroscopy (Bruker II-RAM) was used to differentiate between the various chemical bonds of the prepared powders.

The absorbance spectra of the MB solutions were measured by a UV–vis spectrophotometer (V- 630, JASCO) in the wavelength range [500–800 nm]. In order to apply the photodetector, a UV lamp (λ = 250

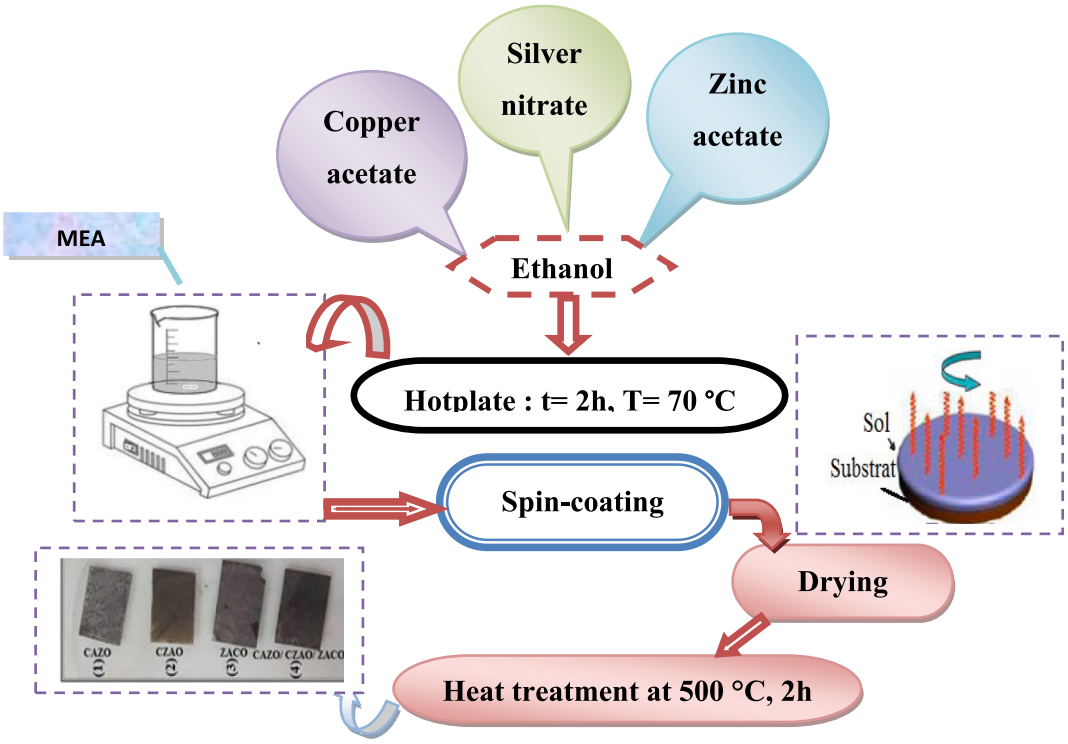

Fig. 1. Schematic presents the stages of preparation of thin layers by the spin-coating method.

nm, 6 W, VL-6C, Vilber Lourmat), was used for illumination. A microam parameter (MS406) was used for measuring the current through the samples associated with a generator (changing the bias voltage from 0 to 12V) with direct and indirect polarization.

3. Results and discussion

3.1. X-ray diffraction (XRD)

The results of the X-ray diffraction for the samples prepared using the spin-coating technique (Fig. 2) showed that they have a polycrystalline structure according to the diversity of the phases. The effect of the percentage of doping with the used elements (Zn, Ag and Cu) is visible in the nature of the crystal structure, as a significant change is observed in the intensity of the diffraction peaks after doping. When the crystal structure was changed (ZnO, Ag_2O, and CuO), the intensity of the peaks decreased at the main lattice orientations and increased in other orientations.

The intensity decreased for all peaks of the multilayer sample (CAZO/CZAO/ZACO). This result confirms that the addition in specific proportions led to an increase in the crystallization of the membrane, i. e., it led to an improvement in the crystal structure. On the other hand, it was noticed a shift in the angles in each diffraction spectrum, which confirms the alternative incorporation of silver, zinc, and copper doped elements (with ionic radii $Ag^{+2} = 1.26$, $Zn^{+2} = 0.74$, and $Cu^{+2} = 0.73$ Å) in the corresponding crystal structure.

The peaks of the three phases dominant in all samples can be clearly distinguished in the diffraction spectra of the ZnO wurtzite phase (JCPDS 00-036-1451), which corresponds to the (100), (002) peaks, while peaks (110), (002), (200), (−112), (−202) and (020) belong to the monoclinic phase CuO (JCPDS 00-041-0254) [47]. The appearance of atomic growth with the dominant and characteristic crystalline directions of the Ag_2O monoclinic phase and the most characteristic trend was (200) and (002) (JCPDS 00-051-0945) [20]. We also noticed the appearance of a prominent peak at an angle of 38.5° corresponding to the Cu_2O phase (JCPDS 0.5–0.667).

Khan et al. [48] deposited zinc oxide (ZnO) multilayer thin films on a glass substrate using a spin-coating technique. X-ray diffraction confirms that ZnO has a hexagonal wurtzite structure. It is also noted that these multilayer films have a significant effect on the properties of ZnO [48]. The XRD data prepared by Mostafa et al. showed the presence of hexagonal Ag on ZnO in the formation of ZnO thin films and ZnO/Ag thin films.

It is also showed that the crystal size decreases with an increase of the Ag concentration due to the difference in atomic radii between Zn and Ag atoms in the crystal structure composition of Ag-coated ZnO [49]. ZnO/CuO multilayer thin films have also been deposited on amorphous SiO_2/Si substrates using pulsed laser technique by Allabergenov et al. [31]. XRD analysis of the annealed ZnO/CuO films reveal the formation of multiple crystalline defects and modulation of the dominant growth plane, which indicates effective doping for copper atoms in the ZnO lattice. Thus, the near-band emission in ZnO can be controlled by the number of CuO layers [50].

Table 1 presents the results from the structural analysis with the different compounds contained in the prepared samples. Based on the results, the average particle size was approximately obtained. It was found that the sample based on zinc oxide (CAZO) contained a smaller particle size, of about ~31 nm, compared to the samples based on copper oxide (ZACO) and silver oxide (CZAO), which were estimated at about ~37 and ~38 nm, respectively. While for the sample containing multiple layers (CAZO/CZAO/ZACO) an increase in the particle size, reaching about ~43 nm was observed.

Changing the proportions of each of the oxides leads to a distortion of the crystal lattice with a slight shift in the angles and a decrease in the intensity of the peaks. This can be attributed to the merging of defective atoms in the structure due to their different ionic diameters, as they occupy the interstitial sites as well as to the stresses. The grain particle size was determined by the Debye-Scherer and micro-stress equations as follows [40]:

$$D = \frac{0.9\lambda}{\beta \cos \theta} \quad (1)$$

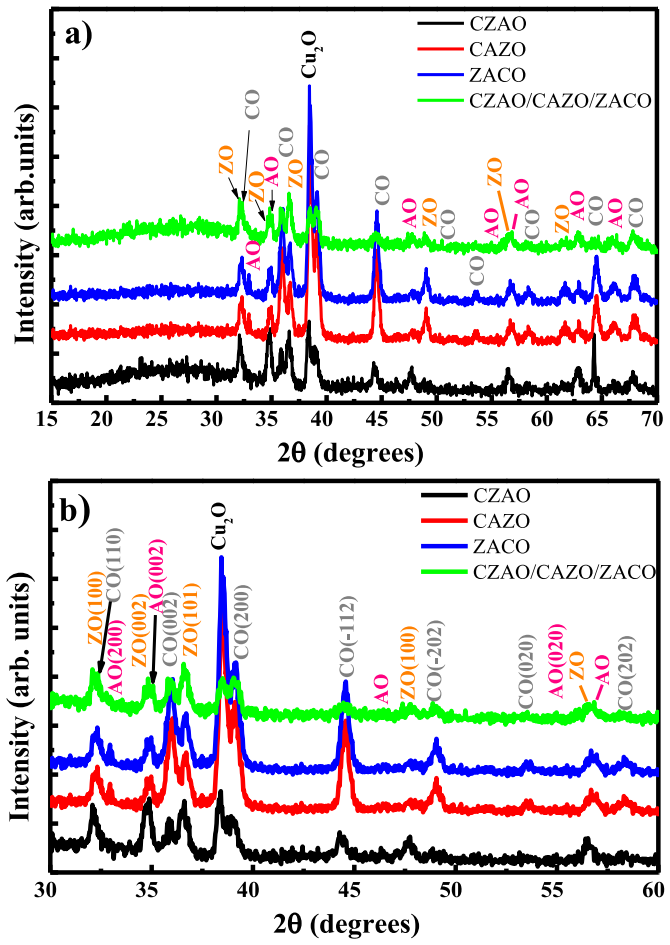

Fig. 2. X-ray diffraction spectra of the prepared layers, ZO:ZnO, CO:CuO and AO:Ag_2O. (a) range (15-70°), (b) range (30-60°).

$$\varepsilon = \frac{\beta}{4\tan\theta} \tag{2}$$

where λ is the wavelength of the anticathode (λ_{Cu} = 1.541 Å), β is the FWHM (half-value width), θ is the diffraction angle and D is the diameter of the particle size.

The calculated values of the network parameter are displayed in Table 2. It is noted that cell parameters (a, b and c) and the size of a cell change with the added ratios (ZnO/CuO/Ag_2O). Where the radius value of Zn^{+2} (0.74 å) and Cu^{+2} (0.73 Å) ions smaller than Ag^{+2} (1.26 Å).

The experimental network parameters are not consistent with the theoretical parameter, which is in the JCPDS file of software instructions (00-036-1451) for zinc oxide, (00-041-0254) Silver oxide and (00-041-0254) copper oxide. Based on calculation, the dimension of the cell changes from one sample to another, and this is due to the contraction and expansion that occurs to the crystal network while adding the elements. While it was confirmed, that cell volume of silver is the largest, ranging between 112 and 175 $Å^3$.

The lattice parameters of the monoclinic structure of CuO and Ag_2O ($a \neq b \neq c$, $\alpha = \gamma = 90° \neq \beta$) were calculated using the following equations [40,41]:

$$d_{hkl} = \frac{1}{\sqrt{\left(\frac{h^2}{a^2} + \frac{l^2}{c^2} - \frac{2hl}{ac}\cos\beta\right)\frac{1}{\sin^2\beta} + \frac{k^2}{b^2}}} \tag{3}$$

The mesh parameter of hexagonal structure materials ($a = b \neq c$, $\alpha = \gamma = 90° \neq \beta$) is connected to the indices (h, k, l) and to the position of the d_{hkl} by the following relation [50]:

$$d_{hkl} = \frac{1}{\sqrt{\frac{4}{3a^2}\left(h^2 + k^2 + hk\right) + \frac{l^2}{c^2}}} \tag{4}$$

As for the volume's cells, it was calculated according to the following relationship [41]:

$$V = abc\left[1 - \cos^2\alpha - \cos^2\beta - \cos^2\gamma + 2\cos\alpha\cos\beta\cos\gamma\right]^{\frac{1}{2}} \tag{5}$$

3.2. Scanning electron microscopy (SEM)

Fig. 3a-d shows the morphological aspects of the CZAO, CAZO, ZACO, and CAZO/CZAO/ZACO multilayer films on the upper surface as observed by scanning electron microscopy. The difference in the doping and the deposition method of the same type or multilayer significantly affects the shape of the upper surface and the size of the grains that make it up. The results are given in Table 3 for the average grain size of the four samples. Following the deposition of the three layers of CAZO, a rough surface was obtained with particles that tended to agglomerate in the form of spherical islands that spread across the entire surface and had a size of less than 505 nm (see Fig. 4).

These fine structures can be explained by the silver grains that are not located within the zinc oxide crystal lattice as they have a larger grain size than the grains, voids, and atomization's present in the ZnO crystal network. Moreover, all the samples clearly show silver granules of large size and a distinctive luminous color [48,49].

When silver doping is used for zinc and copper (Fig. 3b), a porous surface was noticed along the sample with an average pore size of 308 nm, making it more effective and active in the photocatalytic process,

Table 1
Crystallite size and micro-stress rate of samples.

Sample	Phases	(hkl)	2Θ (°)	Θ(°)	FHWβ (°)	β (rad)	D(nm)	ε (%) microstrain
CZAO	ZnO	(101)	36.61	18.30	0.47	0.00817	17.88	0.35528
	Ag_2O	(200)	32.94	16.47	0.16	0.00278	52.03	0.13529
	CuO	(002)	35.87	17.93	0.283	0.00492	29.63	0.21865
		(200)	38.41	19.20	0.31	0.00539	27.25	0.22254
CAZO	ZnO	(101)	36.701	18.35	0.308	0.00536	27.26	0.23215
	Ag_2O	(200)	32.95	16.47	0.12	0.00209	69.20	0.10147
	CuO	(002)	36.04	18.02	0.349	0.00607	24.03	0.26821
		(200)	38.45	19.22	0.253	0.0044	33.38	0.18142
AZCO	ZnO	(101)	36.70	18.35	0.283	0.00492	29.70	0.21330
	Ag_2O	(200)	32.94	16.47	0.121	0.0021	68.87	0.10232
	CuO	(002)	36.028	18.01	0.335	0.00583	25.19	0.25760
		(200)	38.449	19.22	0.3	0.00522	27.98	0.21513
Multi-layer	ZnO	(101)	36.58	18.29	0.335	0.00583	25.06	0.25338
	Ag_2O	(200)	32.938	16.47	0.09	0.00157	92.12	0.07610
	CuO	(002)	35.96	17.98	0.326	0.00567	25.72	0.25113
		(200)	38.51	19.25	0.257	0.00447	32.87	0.34921

Table 2
The lattice parameters (a, b, c) and volumes cells.

Samples	Phases	2θ (°)	hkl	$d_{hkl} = n\lambda/2\sin\theta$ (Å)	a (Å)	b(Å)	c(Å)	Volume of cell (Å^3)
CZAO	**ZnO**	32.08	(100)	2.78782718	3.219105	3.219105	5.178279	55.686
		34.661	(002)	2.58591395				
	CuO	53.201	(020)	1.72031478	4.6837328	3.440629	5.072957	89.0269718
		35.869	(002)	2.50154618				
		38.965	(200)	2.30961403				
	Ag_2O	32.803	(200)	2.72801414	5.721119	5.1432129	5.393105	175.114434
		34.86	(002)	2.57160645				
		54.941	(020)	1.66987557				
CAZO	**ZnO**	32.09	(100)	2.78698124	3.218128	3.218128	5.160140	55.4576009
		34.742	(002)	2.58007019				
	CuO	53.465	(020)	1.71244116	4.663721	3.424882	5.056192	87.9492611
		35.992	(002)	2.49327888				
		39.139	(200)	2.29974595				
	Ag_2O	32.925	(200)	2.71818395	5.700504	3.341826	5.375179	112.994578
		34.98	(002)	2.5630588				
		54.904	(020)	1.67091336				
AZCO	**ZnO**	32.08	(100)	2.78782718	3.2191053	3.2191053	5.154820	55.434079
		34.779	(002)	2.57741002				
	CuO	53.507	(020)	1.71119601	4.663721	3.422392	5.051037	87.7957164
		36.03	(002)	2.49073637				
		39.139	(200)	2.29974595				
	Ag_2O	32.925	(200)	2.71818395	5.7005038	3.340368	5.3811408	113.070548
		34.94	(002)	2.56590138				
		54.93	(020)	1.67018395				
Multilayer	**ZnO**	32.08	(100)	2.78782718	3.2188055	3.2188055	5.171828	55.6066213
		34.661	(002)	2.58591395				
	CuO	53.554	(020)	1.70980505	4.673474	3.419610	5.072957	88.289296
		35.869	(002)	2.50154618				
		39.054	(200)	2.30455534				
	Ag_2O	32.802	(200)	2.72809502	5.721289	3.335217	5.363002	112.925891
		35.062	(002)	2.55725212				
		55.022	(020)	1.66760876				

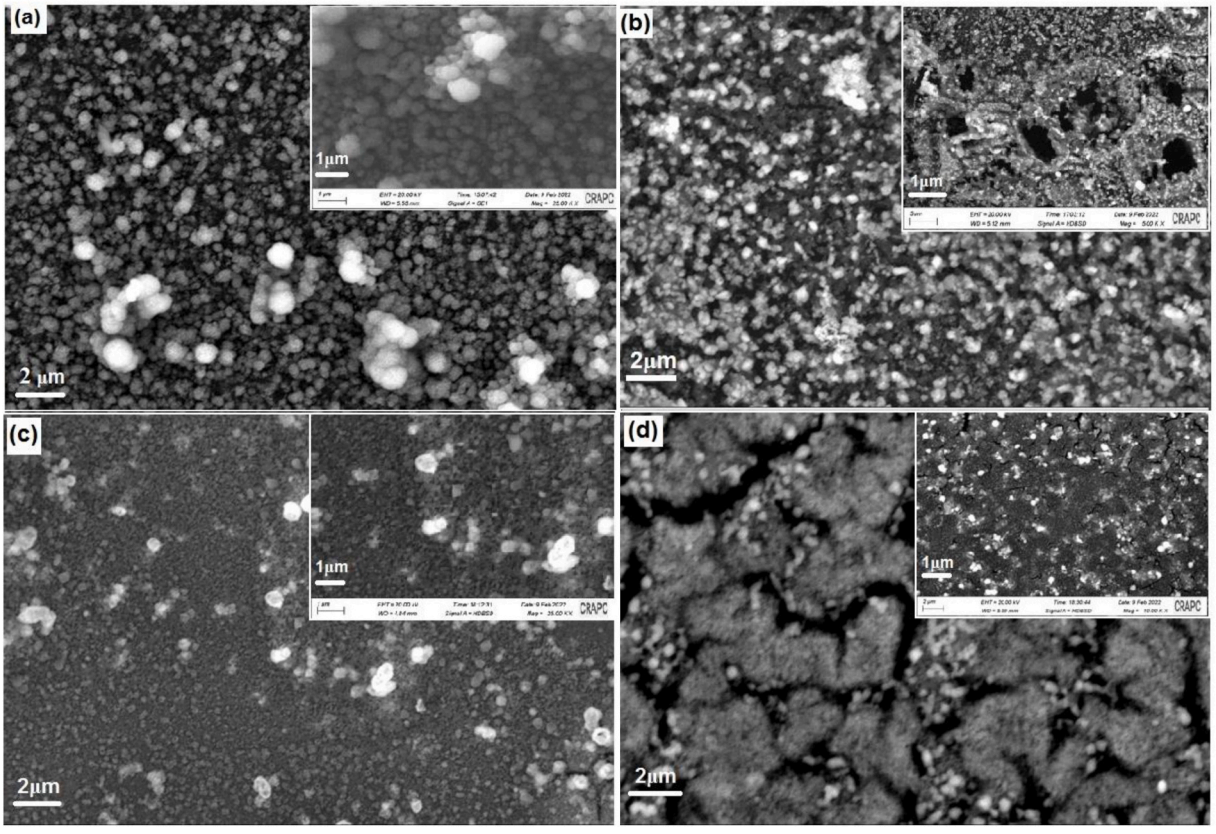

Fig. 3. SEM images of (a) CAZO, (b) CZAO, (c) ZACO and (d) (CAZO/CZAO/ZACO) multilayer surfaces.

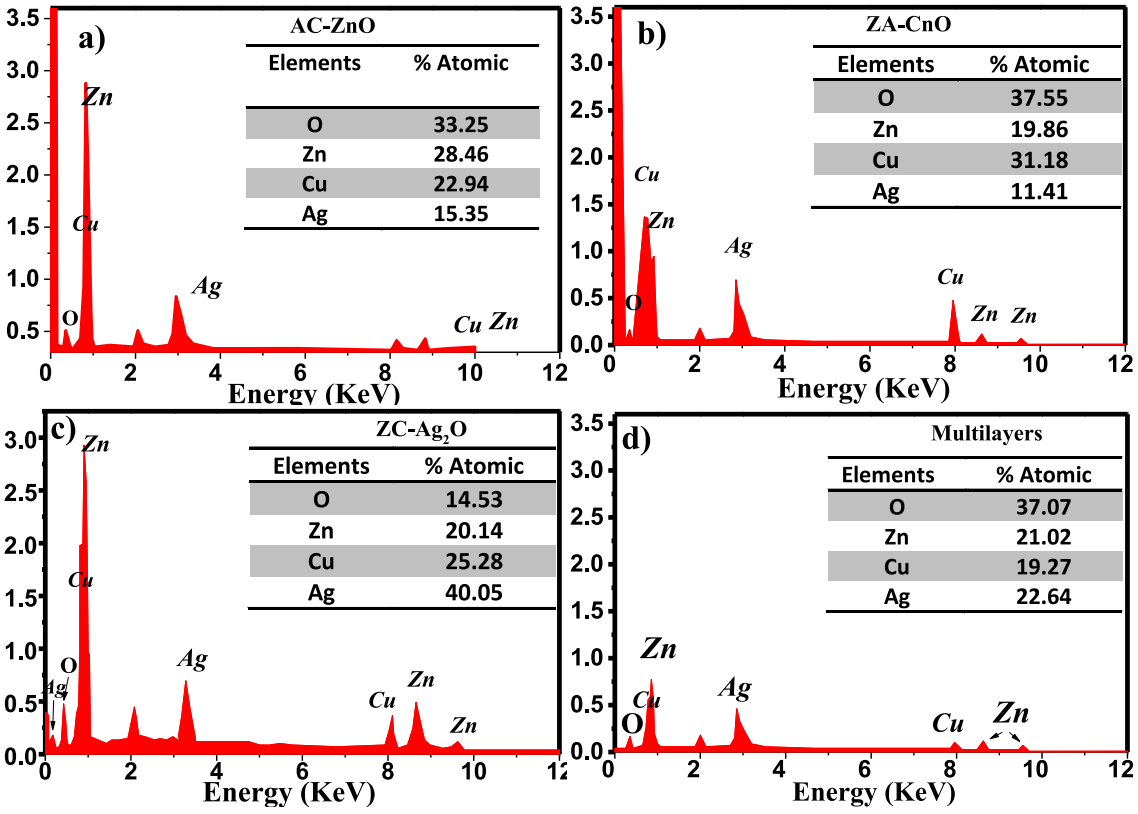

Fig. 4. EDS spectra for (a) CAZO, (b) ZACO, (c) CZAO and (d) CAZO/CZAO/ZACO thins layers.

Table 3
Grain size of all samples calculated from MEB.

Samples	CZAO	CAZO	ZACO	CAZO/ CZAO/ ZACO
Average grain size (nm)	367	98	173	104

and it was less rough than the first CAZO (Fig. 3a), due to the implantation of grains of both zinc and copper within the crystal lattice of silver. This observation was not found in the ZACO sample, which has a surface free of pores with the presence of unique grains of silver on its surface.

The multilayered CAZO/CZAO/ZACO showed a completely different shape from single coatings. It was observed a big change in its lattice, with divisions and the formation of tracks that reached the length of the space between them approximately 3 nm. This is due to the deposition

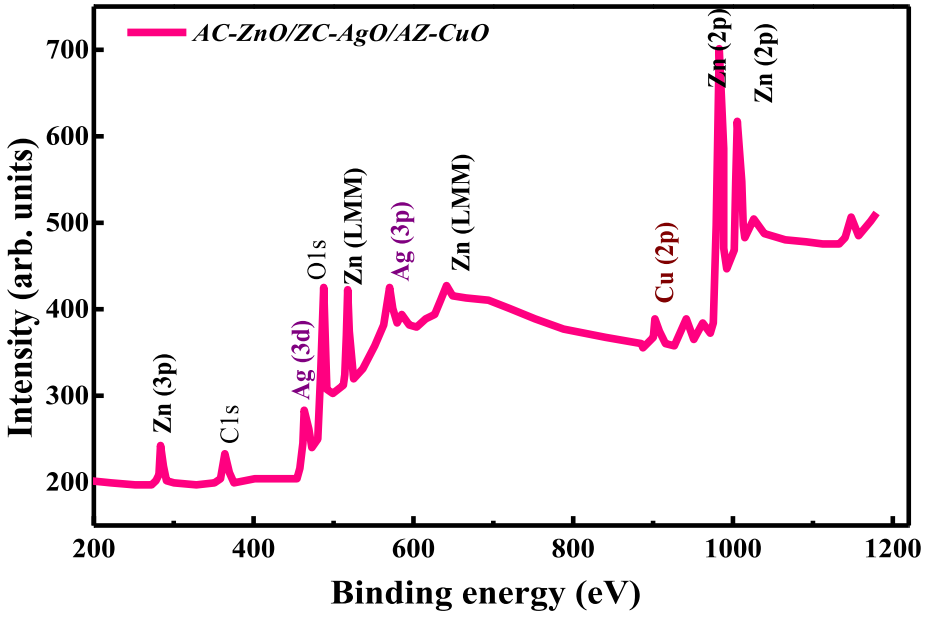

Fig. 5. The XPS spectra of the CZAO/CAZO/ZACO multilayer's.

method, where each layer contains a different type and the presence of the largest number of oxides, which makes it more catalytic and effective than the previous ones (CAZO, CZAO, ZACO).

The results obtained are in accordance to some of the other researcher's works. Khan et al. [48] showed that films were crack-free and had uniformly distributed granular structures. Both micro and nanoparticles of ZnO are present in thin films [48]. SEM images of the ZnO and ZnO/Ag multilayer thin films prepared by Mostafa et al. [49] were clearly the result of a thin layer of ZnO coated with an Ag film, indicating that Ag can modify the morphology of ZnO films [49]. The ZnO/Ag multilayer thin film shows an exceptional potential enhancement compared to that of ZnO thin film [49].

3.3. X-ray photoelectron spectroscopy

The chemical composition of the multilayer sample was additionally analyzed using XPS and shown in Fig. 5. The full scanning spectrum revealed confirmation of the presence of elements C, O, Zn, Ag and Cu within the CZAO/CAZO/ ZACO multilayer sample. Zn 2p consists of two peaks positioned at 984.53 and 1007.31 eV for Zn $2p_{3/2}$ and Zn $2p_{1/2}$ [51]. While the peaks with energies of 464.36 and 571.77 eV correspond to Ag $3d_{5/2}$ and Ag $3d_{3/2}$, respectively, and belong to Ag+ in the Ag_2O phase. In addition, the Cu 2p binding energy was found at 906.58 eV [52]. The binding energy peaks for O1s were at 487.15 eV, while the carbon peak came from adventitious carbon present on the surface of the sample [51]. Based on this study, it can be concluded that the compound is composed of three oxides CuO–AgO–ZnO.

3.4. IR spectra

It was noted from the infrared spectra of the four samples shown in Fig. 6 in the range of (400–4000) cm^{-1}, that there is a wide absorption band in the range of 3753 cm^{-1}corresponding to the O–H stretch-vibration bond caused by water molecules [51]. While the band is in the (1653–1556) cm^{-1} range, it corresponds to the O–H bond curvature vibration generated by the atmosphere [52]. As for the absorption band located in the range of (404, 411.79, and 495.54 cm^{-1}) corresponding to Zn–O, there are vibration bonds present in the ZnO lattice [53,54].

There is an offset in the value of the CuO vibration lines that appear in the range of (429, 491, 462, and 483 cm^{-1}), corresponding to the spectra of the four samples CAZO, CZAO, ZACO, and CAZO/CZAO/ ZACO, respectively. The observed shift of the band is due to the doping ratio with Zn^{+2}, Cu^{+2}, and Ag^{+2} ions occupying the corresponding main lattice sites. While the absorption bands of the Ag–O vibration bond appear at (665 and 881) cm^{-1}. In the case of the CZAO/CAZO/ ZACO multilayer sample, it is significantly different from the other samples, and the clear manifestation of vibrational lines of zinc, copper and silver oxides made it the most efficient sample in photocatalysis.

3.5. Optical properties

3.5.1. Absorbance spectrum

All the measurements of the absorbance spectrum are in the wavelength range (200-900e.V) nm for all the four types of prepared films. Figure (7a) shows that the absorbance increases significantly in samples CZAO and CZAO/CAZO/ZACO (multilayer), with the same behavior. The absorbance decreases in samples CAZO and CZAO (70%–80 %). Figure (7b) shows that the absorbance of the prepared films generally begins to increase gradually with increasing energy of incident photons. This growth occurs rapidly when the incident photon energy equals or exceeds the value of the optical energy gap of all the prepared films, indicating the occurrence of direct electron transmissions.

One reason is the increase in the density of the levels formed by the impurity atoms in the similar material between the valence and conduction bands that act as a ladder for the transfer of electrons absorbing photons with energies less than the value of the optical energy gap of the prepared films and thus the transition occurs, which indicates that the doping and change in the type of layers for the same sample improved the crystal structure and reduced the optical energy gap, thus reducing the optical transmittance and increasing the absorbance [54].

When compared to the absorbance of the prepared films (CZAO, CAZO and ZACO), the prepared multilayer films achieved the highest absorbance, followed by the prepared silver doped copper and zinc films with a percentage of doping of 50 %, as the absorbance of these two samples reached more than 80 % for the range of wavelengths located within the visible region of the electromagnetic spectrum (400–800) nm.

Optical absorption spectra were measured using UV–Vis. In other study [48] it was shown that the average transmittance in the visible region for all ZnO films is 80 % which is good for the solar spectra. It was

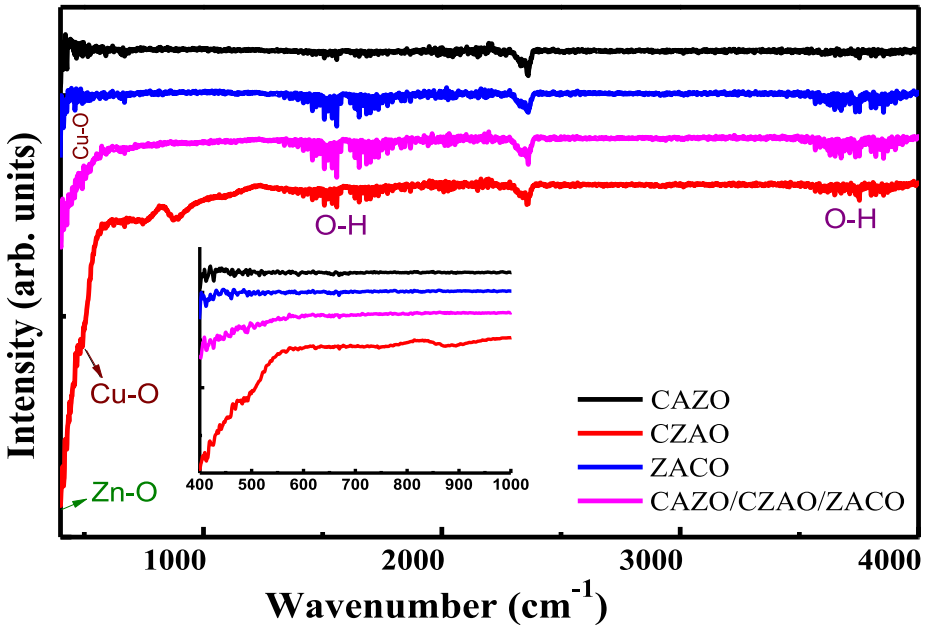

Fig. 6. Infrared spectrum of samples CAZO, CZAO, ZACO and multilayer (CZAO/CAZO/ ZACO) treated at 500 °C.

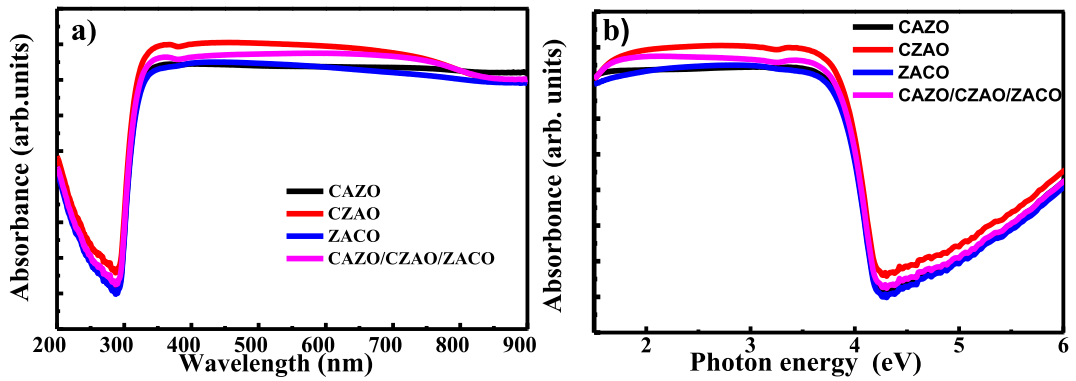

Fig. 7. Absorbance values change with (a) the energy of the incident photons and (b) the wavelength as a function of the prepared films.

found that the performance of the multi-layer as a transparent conductive material is better than the single layer of ZnO [48].

When analyzing the optical properties of the grown thin films in the case of ZnO thin films and ZnO/Ag thin films by Chen et al. [55], it was observed that all the prepared films had excellent transmittance in the visible spectrum. The transmittance of the Ag-coated ZnO film is close to 79 % for 430–700 nm, which is lower than that of the uncoated ZnO thin film. This may be attributed to the fact that ZnO films contain more voids than ZnO/Ag films. In addition, the significant decrease in UV transparency of the multilayer film may be due to scattering from pores and other defects that are abundant in the films [55]. Thus, this work provides a low-cost, environmentally friendly, and well-drained material for solar cell applications.

3.5.1.1. Refractive index (n). The refractive index was calculated from the relationship [10]:

$$n = \left[\left(\frac{1+R}{1-R}\right)^2 - \left(1+k^2\right)\right]^{\frac{1}{2}} \tag{6}$$

where R is the reflectivity and K represents the damping factor.

The refractive index (Fig. 8a) is high in samples CZAO/CAZO/ZACO, followed by sample CZAO, compared with samples CAZO and CZAO. The reason for this high value of n is that the process of doping with zinc and copper led to the addition of impurity atoms within the crystal structure of the silver films.

The increase in the refractive index is due to an increase in densification resulting from an improvement in the crystal structure of the films prepared for the two samples. This increases the intensity of the reflected rays, thereby increasing the refractive index (Fig. 8b). Then, at longer wavelengths, the refractive index values of the same two samples begin to slowly decrease. This means that the reflectivity of the film decreases.

3.5.2. Dielectric constant (ε)

It is defined as the amount of absorption in the energy of the incident photons due to the polarization of the charges of the membrane material due to the electric field complex of electromagnetic radiation as a result of passing through it, and it is of two types: the real part dielectric constant (ε_r) and the imaginary part dielectric constant (ε_i).

The values of the real and imaginary dielectric constants were calculated from the two equations [50–52].

$$\varepsilon_r = n^2 - k^2 \tag{7}$$

$$\varepsilon_i = 2nk \tag{8}$$

It can be seen from Figure (9a) that high values in samples CZAO/CAZO/ZACO and CZAO are similar to and affected by the behavior of the refractive index. The reason for this is the high density of the dipoles generated by the difference in impurities of the pure film material, which increases the values of optical polarization and refractive index of the low photon energies, respectively, and produces an increase in the value of the dielectric constant in its real part.

The imaginary part of the dielectric constant Figure (9b) represents how much the material absorbs from the electromagnetic radiation falling on it as a result of the interaction of the electric vehicle's radiation with the charges of the material. Its polarization ε_i is high in regions with high wavelengths and is most evident in the behavior of a multilayer sample, after which its higher values move lower as the curve's crests creep towards lower photonic energies (short wavelengths).

This is because unclean atoms have gotten into the crystal structure of the pure membrane material. This effect has induced new levels to form within the forbidden energy gap.

3.5.3. Optical energy gap

The direct optical energy gap was calculated by plotting the graph between photon energy $h\nu$ and $(\alpha h\nu)^2$ for all the prepared films using

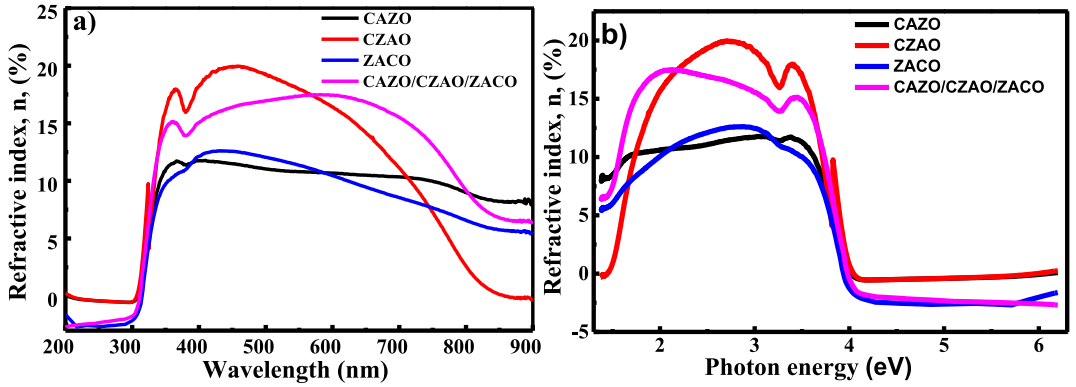

Fig. 8. Refractive index values change with (a) the energy of the incident photons and (b) the wavelength as a function of the prepared films.

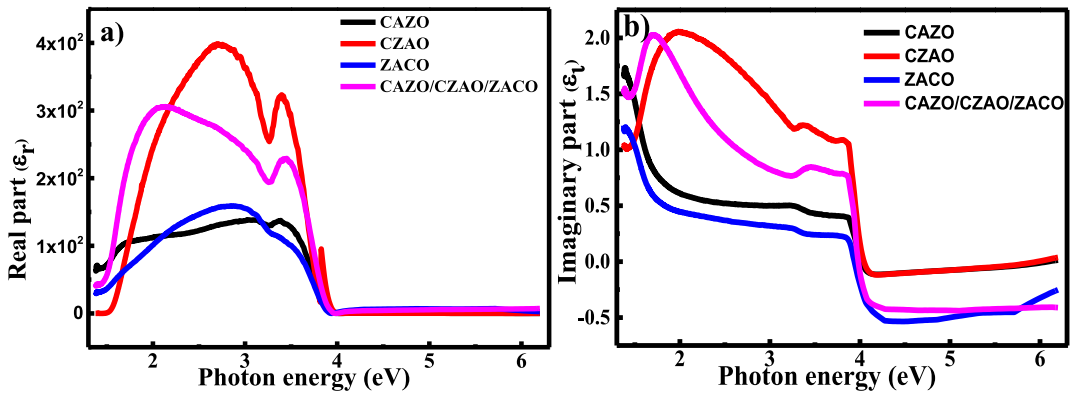

Fig. 9. Variation of the real and imaginary dielectric constant values as a function of the energy of the incident photons of the prepared films.

following relationship [49–52]:

$$hv = (\alpha hv)^2 \tag{9}$$

where α is the order of the optical transmission, (hx) energy of the incident photon.

Fig. 10 compares the energy gaps of the three samples, CAZO, CZAO, and ZACO, and enabled us to know the lowest value between them and also the best membrane that can be used as a basic catalyst among the three oxides (zinc oxide, copper oxide, or silver oxide). The photocatalys is a process with the smallest value of 3.76 eV for Zn–Cu co-doped silver (CZAO), 3.81 eV and 3.85 eV for CAZO and ZACO samples, respectively. This discrepancy in the energy gap of the samples can be attributed to the difference in the values of the absorption coefficient, as its increase corresponds to a decrease in E_g.

The CZAO/CAZO/ZACO multilayer process reduced the value of the energy gap further to 3.73 eV. The reason for this reduction is that the position of the three layers led to the addition of new donor levels near the valence band inside the energy gap, which led to the creation of bridges for electrons moving between the valence band and the conduction band, so the number of electronic transitions increased. A change occurred in the location of the Fermi level and its movement towards the valence band in the semiconductor material. Thus, this process improved the structural properties of (CZAO/CAZO/ ZACO) films, and led to obtain a more effective surface.

3.6. Photocatalytic performance

In this work methylene blue was used. A continuous exposure to this dye causes many health problems, so treating water contaminated with this dye is very important [53–59]. For the photocatalysis demonstration, this solution was prepared at a concentration of 4 mg/l. Four beakers with a capacity of 25 ml were prepared. Each sample was immersed in a beaker with a good sealing (to avoid evaporation and increase the concentration of the solution). The solutions were exposed to visible light (Fig. 11).

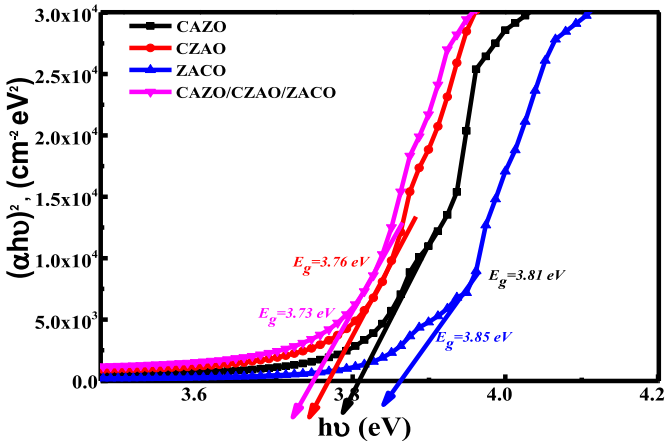

Fig. 10. Energy gap values of the prepared samples.

The photocatalytic activity of the different samples was monitored by a UV–visible spectrophotometer using absorption mode. Absorption spectra measurements are performed hourly on 2.2 ml of solution using distilled water as a reference, and the degradation rate is calculated using the following relationship [60–66]:

$$D(\%) = \frac{C_0 - C}{C_0} \times 100 \tag{10}$$

where C_0 and C are the concentrations, before and after illumination, respectively.

Fig. 12 shows how the degradation rate of methylene blue varies as a function of time exposure to UV light. For CAZO and ZACO samples, it is observed that the absorption spectra do not change significantly (Fig. 12 a and c) and the dissolution rate does not exceed 60 % during exposure to normal light for as much as 5 h (Fig. 13). While it was observed for the CZAO sample (Fig. 12b), the rate of decomposition increased to 71.61 % for the same exposure time (Fig. 13).

The photocatalytic effect is clearly shown (Fig. 12 d), during which the dissolution rate reached 88.96 % for a multilayer sample within 5 h (Fig. 13). From the above, one can observe that the type of sample with three active layers has a significant effect on MB degradation, allowing the development of photocatalysts in an easy, fast, and inexpensive way of preparation.

The use of semiconductors during photocatalysis had a great effectiveness in removing pollutants and partially removing the products of the dissolution of pigments. This process results in hydroxyl radicals when irradiating the catalyst in the presence of water and air, and since it is a process conjugated with oxygen, it is able to accomplish the decomposition process of organic pollutants and convert them into carbon dioxide, water, and some other non-toxic compounds.

Moreover, the adsorption process involves both the outer surface area and the inner pores compared with the samples ZACO and CAZO (Fig. 12 a-c). Oxidation reactions appeared more in the sample (CZAO/CAZO/ZACO) (Fig. 12 d), which was decomposed in a shorter period of time (Fig. 13). This is due to the more effective surface. Its shape was previously shown in the SEM images, as the catalysis did not only contribute to the surface, but the existing cracks contributed to an increase in the support of the three layers, starting from the brightening of the thin films until reaching the glass substrate which made it possible to create the largest number of pairs and thus faster degradation.

The process depends on the generation of radicals (• OH) from the production of the largest number of pairs (e^-/h^+) leading to the

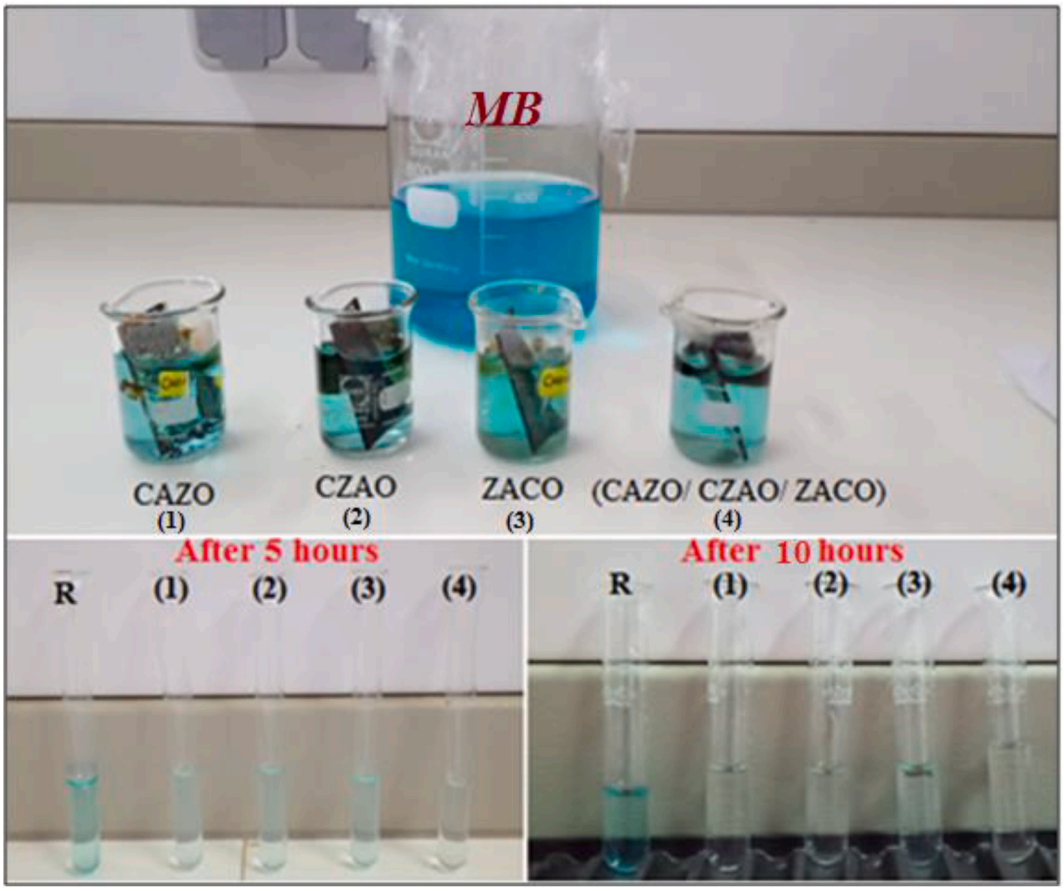

Fig. 11. Image showing the photocatalytic activity process.

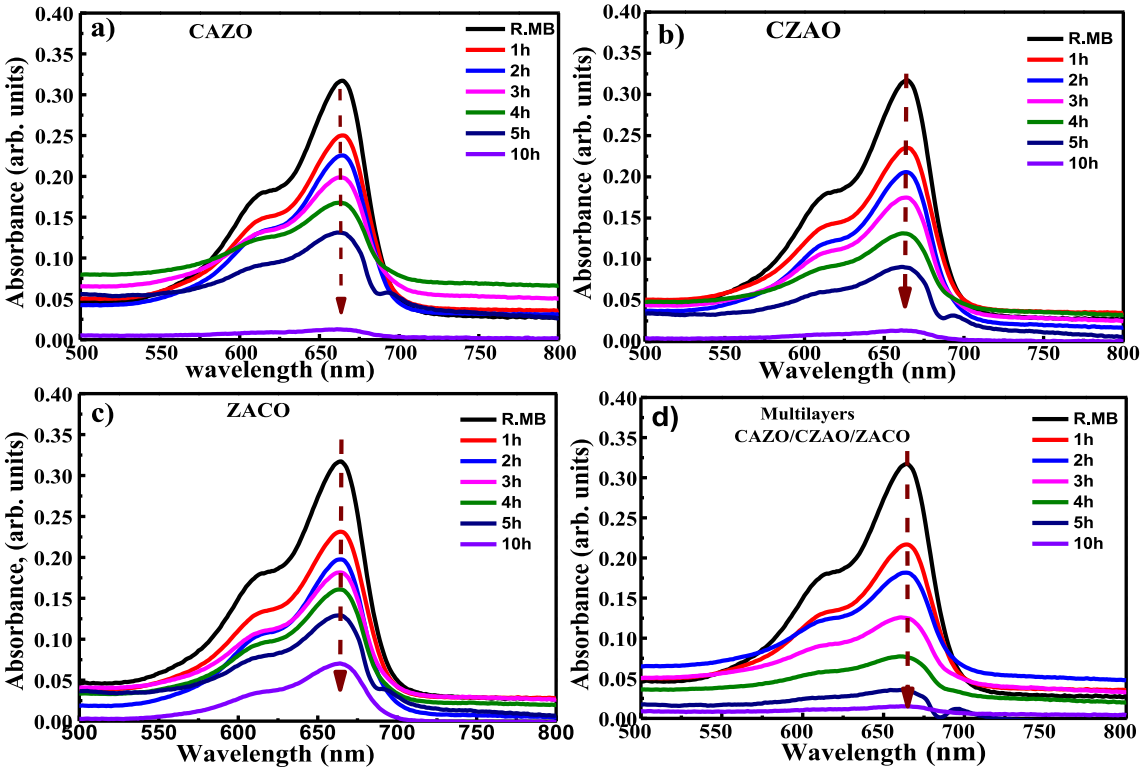

Fig. 12. Absorbance spectra showing the effect of layers a): CAZO, b): CZAO, c): ZACO and d): (CAZO/CZAO/ZACO) multilayer.

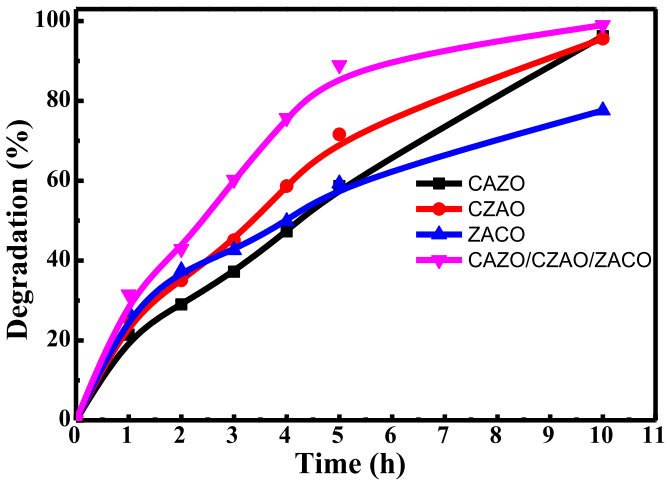

Fig. 13. Degradation rate of MB versus UV exposure time for CAZO, CZAO, ZACO and (CZAO/CAZO/ZACO) multilayer.

deposition of active layers based on low-gap materials (ZnO: 3.4 eV, CuO: 1.2 eV) in the network. Crystalline AgO (the sample CZAO) increases the number of generated electrons involved in reducing O_2, giving the solution a white color. H^+, H_2O, and OH^- react to form a larger number of •OH, which acts as the main oxidant that leads to the deterioration of the dye in MB solution due to the high surface area of the sample (Fig. 12b) [65,66].

Among these materials, CZAO/CAZO/ZACO is a better choice because it provides a large surface to adsorb pollutants. It has a better ability to respond to several external stimuli such as ionic strength of the medium, temperature, and pH. Thin layers can be reused by recycling readily by burning it at the same processing temperature, which is 500 °C. CZAO/CAZO/ZACO particles during repeated recycling remain stable due to the interconnected network and are not degraded. Multilayers proved competent adsorbents for the elimination of toxic dyes from aqueous medium. The sample has been successfully applied for the removal of toxic metal ions from MB solution but less effective than using it the first time. The gradient of the solution reached 55.23 % in a time of 5 h (Fig. 14 d.e), while the decomposition in the first time was approximately 89 % in a time of 5 h.

3.7. Ultraviolet photodetection application

The manufacture of the optical detection based on the heterogeneous structure is an effective way to enhance the sensitivity and speed of the device. This type of structure does not only provide excellent electrical properties, but also gives mechanical stability required for flexible electronics applications [68]. The specifications of the current voltage in the dark and under UV rays were obtained at 254 nm and 0–10 V to examine the UV detectors based on the thin and multilayers layers (Fig. 15).

Through the shape it is noted that the dark current of the samples was relatively low and that is when applying 12 voltages 11.416, 12.333, 12.874 and 14.215 A for all ZACO, CAZO, CZAO and CZAO/CAZO/ZACO compared to the increase in all samples under UV light, as it reached 12.5 and 13.123, 16.897 and 20.549 A, respectively. These results clearly show that the UV detection device based on the multiple layers display the maximum value of the image stream, which means that the optical conductivity of this sample is higher than layers separately [67].

To evaluate the performance of the photodetector, the ratio between the current measured under illumination I_{ph} and that measured in the dark *I*dark was calculated which represents the responsivity R(λ) [68]. It is possible to compare the quality of a device's response to incident light. The higher this value, the more the detector generates charge carrier by absorbing photons. Another property that makes it possible to evaluate is the performance of the detectivity (D).

It is a method for measuring the sensitivity of the photodetector [69]. This property is derived from the quantum efficiency and is directly related to the generated photocurrent by the photodetector with the optical power of the incident light. The value of sensitivity, responsivity and detectivity are given by the following relations [69,70]:

$$S = I_{Ph}/I_{dark} \tag{11}$$

$$R = I_{Ph}/P_{inc} \tag{12}$$

$$D = R \Big/ (2eI_{dark})^{1/2} \tag{13}$$

where I_{ph} is the photo-current generated by the photodetector as a result of optical excitation and P_{inc} is the optical power of the incident light.

Through Table 4, the discovery, responsivity and the highest sensitivity that was observed in the sample with multilayers can be explained by the increase in the lighting stream in samples in the presence of ultraviolet radiation. The latter increases with increase in the number of free electrons and thus the number of holes in which oxygen ions are held [71].

Excellent photoresponsivity and sensitivity were obtained for the CZAO/CAZO/ZACO sample based on the multilayer photodetectors, where the photocurrent increased to its maximum with increasing levels, which were under ultraviolet irradiation compared with the other samples ZACO, CAZO, CZAO. The superiority of the illumination current over the dark current indicates that the UV sensitivity of the structures in the current study could be used for UV detectors. The overall performance of the device also ensured a wide potential in optoelectronics applications [72].

3.8. Mechanism of UV photodetection

Its basic structure for photodetectors consists of semiconductor materials which are connected to an electrical circuit by means of two electrodes and allow the application of a voltage on the terminals of the material for the production of an electric current.

In the dark, when an external electric field is applied, the oxygen molecules in the atmospheric air O_2 (*gas*) are adsorbed on the surface of the layers as negatively charged ions by capturing the free electrons in the conduction band of the sample [72,73]. The formation of a large number of ionized oxygen on the surface of the thin films leads to the formation of charge depletion region near the surface, which leads to separation of charge carriers and reduced recombination [74].

Whereas, under the influence of the light beam, each incoming photon transfers its energy $h\nu$ to an electron from the active material located in the valence band, so it absorbs it and moves to the conduction band so that its energy is greater than or equal to the width of the band gap E_g for semiconductors (hv > Eg). This process results in the generation of electron-hole pairs that modulate the conductivity of the absorbent layer and thus the conductivity of the semiconductor [74].

This effect results in an increase in the current (I) in the circuit, due to the generation of photo current I_{pho}. Adsorbed oxygen ions (O_2^-) are also discharged through surface electron hole recombination on the nanosurface. To improve the speed and sensitivity of the photodetector, silver, copper and zinc oxides are very suitable materials due to their fast charging ability and high dynamic stability.

These materials also possess a suitable forbidden bandwidth when combined which enhances electron transfer. In addition, the sample response rate and carrier concentration in the multilayer structure can be significantly improved by contributing to an increased number of oxygen vacancies generated, which improves the photocurrent of the photodetectors significantly over the rest of the samples.

The three ions are replaced by Zn^{2+}, Cu^{2+}, Ag^{2+} in the lattice easily, which results in the release of electrons to maintain its electrical

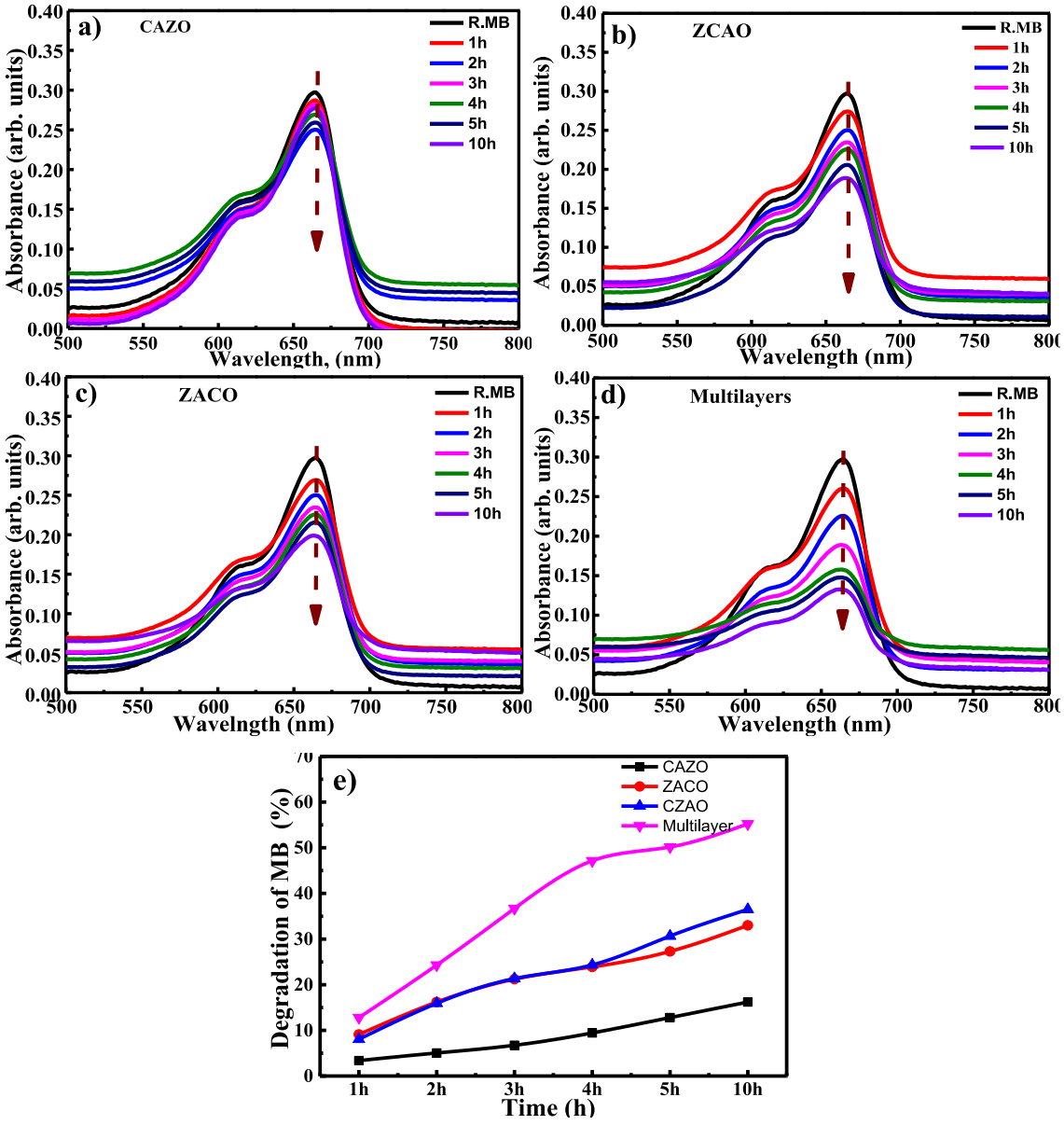

Fig. 14. Absorbance spectra after recycling for the photo degradation. a): CAZO, b): CZAO, c): ZACO and d): (CZAO/CAZO/ZACO) multilayer and e) Degradation rate for the samples.

neutrality. Thus increases the response of the sample and the concentration of free electrons and reduces the resistance of a substance (Fig. 16). Then, the adsorbed oxygen ions O_2 (*ad*) combine with the photo-generated holes (h^+) and produce oxygen molecules O_2 (*gas*), which are then adsorbed from the surface of the nanostructure [75]. Since the photo-generated electrons (e^-) adhere to any electrode electric current, this leads to the formation of a photocurrent I_{ph}. The reaction that takes place can be summarized according to the following equations [73–76]:

$$O_2\,(gas) + e^- \rightarrow O_2^- \quad (14)$$

$$\text{AZCO/CAZO/CZAO} + h\upsilon \rightarrow e^- + h^+ \quad (15)$$

$$O_2^- + \text{h}^+ \rightarrow \text{O}_2 \quad \text{(gas)} \quad (16)$$

4. Conclusion

Active thin films of multilayers CZAO/CAZO/ZACO, CAZO, CZAO, and ZACO prepared by the spin-coating method were deposited on glass substrates. The results of XRD proved that the samples are polycrystalline, and the effect of doping was evident through the intensity of the phases and the alternative incorporation of the doped elements in the crystal structure. Its topography analysis by SEM shows that samples CAZO, CZAO, ZACO, and CZAO are more porous than CAZO and ZACO. The material also has a lower grain size of (98 and 104) nm for CZAO and CZAO/CAZO/ZACO, respectively, the latter having an improved effect on the structural properties and providing a wider active area. The resulting phases were confirmed after layer deposition and identified as ZnO–Ag_2O–CuO composites based on the results of EDS and XPS measurements. The highest absorbance was recorded by the multilayer films, followed by CZAO, as it reached more than 80 % for the wavelengths located in the visible region (400–800) nm. This study also showed that grafting the silver film with zinc and copper leads to a change in the optical properties of the film, and this was evident through

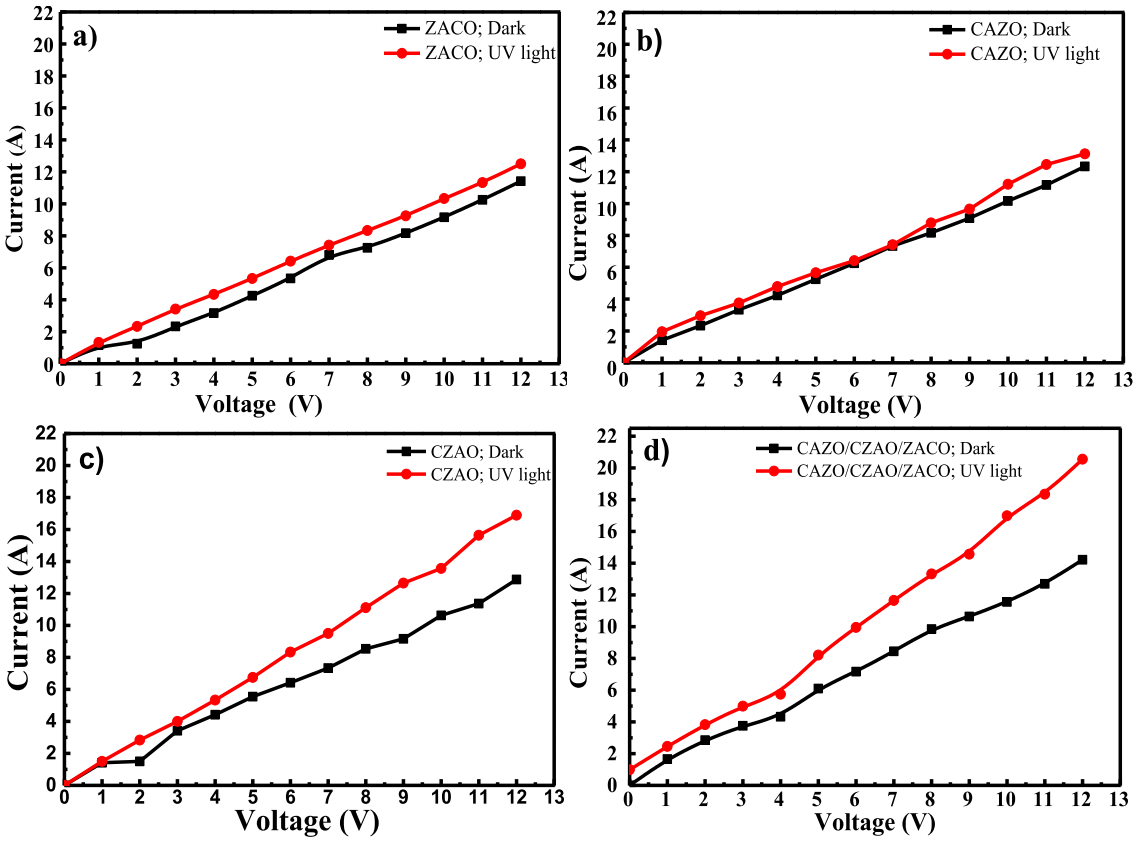

Fig. 15. Current measured as a function of voltage in darkness and under UV light for (a) CAZO, (b) ACZO, (c) CZAO, (d) CZAO/CAZO/ZACO.

Table 4
The characteristics photodetectors of ZACO, CAZO, CZAO and CZAO/CAZO/ZACO measured at 12 V.

Samples	Sensitivity	Responsivity (A/W)	Detectivity
ZACO	1.09495	2.08333	0.436
CAZO	1.06403	2.18717	0.44038
CZAO	1.31249	2.81617	0.55499
CZAO/CAZO/ZACO	1.4456	3.42497	0.64234

the optical constants, where the value of the optical energy gap decreased compared with CAZO and ZACO. On the other hand, we obtained a lower value for the energy gap for the multilayer sample. It also takes the higher values of the refractive index and the values of the real and imaginary dielectric constants, and the preparation with multiple layers leads to an increase in the crystal defects of the film. The results of the photocatalytic activity indicate that the CZAO/CAZO/ZACO multilayer sample is the best and most effective with a photolysis rate of 88.96 %, followed by the CZAO sample with a degradation rate of 71.61 % within a time of 5 h. Sensitivity, responsivity and detectivity of light during photodetection application have proven that the presence of UV light increases the number of holes besieged by oxygen ions and causes

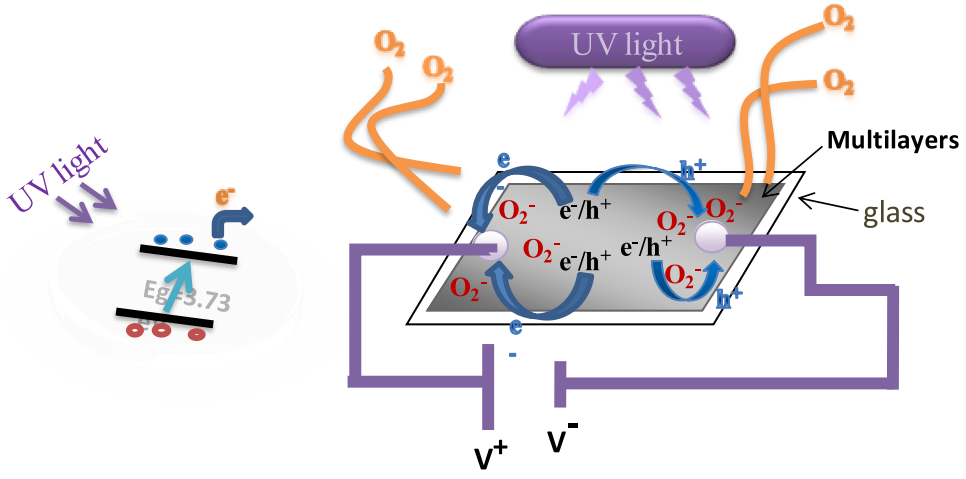

Fig. 16. Mechanism of UV photo-detection of multi-layers based on CZAO/CAZO/ZACO.

more free electrons to contribute to optical current production, particularly for the multilayer film.

Funding

Not applicable.

Declaration of interests

The authors declare that they have no known competing financial interests or personal relationships that could have appeared to influence the work reported in this paper.

Acknowledgment

We acknowledge the support by the German Research Foundation and the BTU Cottbus-Senftenberg.

We acknowledge the Princess Nourah Bint Abdulrahman University Researchers supporting Project Number (PNURSP2023R404), Princess Nourah Bint Abdulrahman University, Riyadh, Saudi Arabia.

References

[1] R. Mahmoodi, N. Mohammad, M. Taghizadeh, A. Taghizadeh, J. Abdi, B. Hayati, A. A. Shekarchi, Bio-based magnetic metal-organic framework nanocomposite: ultrasound-assisted synthesis and pollutant (heavy metal and dye) removal from aqueous media, Appl. Surf. Sci. 480 (2019) 288–299, https://doi.org/10.1016/j.apsusc.2019.02.211.

[2] D. Bouras, A. Mecif, R. Barille, A. Harabi, M. Zaabat, Porosity properties of porous ceramic substrates added with zinc and magnesium material, Ceram. Int. 46 13 (2020) 20838–20846, https://doi.org/10.1016/j.ceramint.2020.05.114.

[3] Zhenke Li, G. Wang, C. Liang, A. Zhang, Synthesis of cyclotriphosphazene-containing polymeric nanotubes and their use as metal-free photocatalysts for methylene blue degradation, Appl. Surf. Sci. 347 (2015) 541–547, https://doi.org/10.1016/j.apsusc.2019.02.211.

[4] D. Bouras, M. Rasheed, Comparison between CrZO and AlZO thin layersand the effect of doping on the lattice properties of zinc oxide, Opt. Quant. Electron. 54 (2022) 824, https://doi.org/10.1007/s11082-022-04161-1.

[5] I. Khan, K. Saeed, I. Zekker, B. Zhang, A.H. Hendi, A. Ahmad, S. Ahmad, N. Zada, H. Ahmad, L.A. Shah, T. Shah, I. Khan, Review on methylene blue: its properties, uses, toxicity and photodegradation, Water 14 2 (2022) 242, https://doi.org/10.3390/w14020242.

[6] B. Lellis, C.Z. Fávaro-Polonio, J.A. Pamphile, J.C. Polonio, Effects of textile dyes on health and the environment and bioremediation potential of living organisms, Biotechnol. Resear. Innov. 3 2 (2019) 275–290, https://doi.org/10.1016/j.biori.2019.09.001.

[7] M. Fellah, N. Hezil, D. Bouras, A. Montagne, A. Obrosov, W. Jamshed, R. W. Ibrahim, A. Iqbal, S. M El Din, H.A. El-Wahed Khalifa, Investigating the effect of milling time on structural, mechanical and tribological properties of a nanostructured hiped alpha alumina for biomaterial applications, Arab. J. Chem. 16 (2023), 105112, https://doi.org/10.1016/j.arabjc.2023.105112.

[8] M. Fellah, N. Hezil, D. Bouras, A. Obrosov, A. Samad Mohammed, A. Montagne, A. Abd-Elmonem, S. M El Din, S. Weiß, Structural, mechanical and tribological performance of a nano structured biomaterialCo-Cr-Mo alloy synthesized via mechanical alloying, J. mater. Sres. technol. 25 (2023) 2152–2165, https://doi.org/10.1016/j.jmrt.2023.06.031.

[9] K. Velusamy, S. Periyasamy, P. Ponnusamy, S. Kumar, N. Dai-Viet Vo, N. Vo, J. Sindhu, D. Sneka, B. Subhashini, Advanced techniques to remove phosphates and nitrates from waters: a review, Environ. Chem. Lett. 19 (12) (2021) 3, https://doi.org/10.1007/s10311-021-01239-2.

[10] M. Jaishankar, T. Tseten, N. Anbalagan, B.B. Mathew, K.N. Beeregowda, Toxicity, mechanism and health effects of some heavy metals, Interdiscipl. Toxicol. 7 2 (2014) 60–72, https://doi.org/10.2478/intox-2014-0009.

[11] Q. Ma, G. Georgiev, P. Cebe, Constraints in semicrystalline polymers: using quasi-isothermal analysis to investigate the mechanisms of formation and loss of the rigid amorphous fraction, Polymer 52 (2011) 4562–4570, https://doi.org/10.1016/j.polymer.2011.08.006.

[12] L. Weijie, X. Fang, D. Wang, F. Tian, H. Wang, D. Fang, J. Li, Band and optical properties of arsenene and antimonene lateral heterostructure by first-principles calculations, Phys. E Low-dimens. Syst. Nanostruct. 134 (2021), 114933, https://doi.org/10.1016/j.physe.2021.114933.

[13] A.N. Kadam, D.P. Bhopate, V.V. Kondalkar, S.M. Majhi, C.D. Bathula, A.V. Tran, S. W. Lee, Facile synthesis of Ag-ZnO core-shell nanostructures with enhanced photocatalytic activity, J. Ind. Eng. Chem. 61 (2018) 7886, https://doi.org/10.1016/j.jiec.2017.12.003.

[14] M. Nie, H. Sun, H.L. Cai, Z.H. Xue, C. Yang, Q. Li, L.Z. Qin, M.Y. Wu, Study on electrocatalytic property of ZnO and Ag/ZnO, Mater. Lett. 271 (2020), https://doi.org/10.1016/j.matlet.2020.127785.

[15] M. Neghabi, A. Behjat, S.M.B. Ghorashi, S.M.A. Salehi, The effect of annealing on structural, electrical and optical properties of nanostructured ZnS/Ag/ZnS films, Thin Solid Films 519 (16) (2011) 5662–5666, https://doi.org/10.1016/j.tsf.2011.03.023.

[16] S.H. Mohamed, Effects of Ag layer and ZnO top layer thicknesses on the physical properties of ZnO/Ag/ZnO multilayer system, J. Phys. Chem. Solid. 69 (10) (2008) 2378–2384, https://doi.org/10.1016/j.jpcs.2008.03.019.

[17] N. Venugopal, M. Anirban, Plasmonics properties of ZnO/Ag/ZnO multilayer thin films, in: Adv. Mater. Res., vol. 585, 2012, pp. 214–218. https://doi.org/10.4028/www.scientific.net/AMR.585.214.

[18] A.M. Mansour, Ali B. Abou Hammad, Ahmed M. Bakr, Amany M. El Nahrawy, in: Silica Zinc Titanate Wide Bandgap Semiconductor Nanocrystallites: Synthesis and Characterization, vol. 14, 2022, pp. 11715–11729, https://doi.org/10.1007/s12633-022-01886-2.

[19] J. Jung, Y. Sup, Y.S. Park, K.H. Kim, W.J. Lee, Properties of AZO/Ag/AZO multilayer thin film deposited on polyethersulfone substrate, Transactions on Electrical and Elec, Materials 14 1 (2013) 9–11, https://doi.org/10.4313/TEEM.2013.14.1.9.

[20] F.Z. Chafi, E. Salmani, L. Bahmad, N. Hassanain, Fares Boubker, A. Mzerd, First principle calculations with SIC correction of Fe-doped CuO compound, Comput. Condensed Matter. 16 (2018), e00304, https://doi.org/10.1016/j.cocom.2018.e00304.

[21] D. Bouras, A. Mecif, A. Mahdjoub, A. Harabi, M. Zaabat, R. Barille, Photocatalytic degradation of orange II by active layers of cu-doped ZnO deposited on porous ceramic Substrates, J. Ovonic Res. 13 (2017) 271–281.

[22] Y. Chen, Review of ZnO transparent conducting oxides for solar applications, IOP Conf. Ser. Mater. Sci. Eng. 423 (2018), 012170, https://doi.org/10.1088/1757-899X/423/1/012170.

[23] A. Di Mauro, ZnO for application in photocatalysis:From thin films to nanostructures, Mater. Sci. Semicond. Process. 69 (2017) 44–51, https://doi.org/10.1016/j.mssp.2017.03.029.

[24] A. Ziashahabi, M. Prato, Z. Dang, R. Poursalehi, N. Naseri, The effect of silver oxidation on the photocatalytic activity of Ag/ZnO hybrid plasmonic/metal-oxide nanostructures under visible light and in the dark, Sci. Rep. 9 (2019), 11839, https://doi.org/10.1038/s41598-019-48075-7.

[25] A. El Hat, M. Rouchdi, A. Hadri, C. Nassiri, F.Z. Chafi, B. Fares, L. Laanab, N. Hassanain, H. Labrim, A. Mzerd, Effects of sulfur concentration on structural, optical and electrical properties of Tin Oxide thin films deposited by spray pyrolysis technique, J. Supercond. Nov. Magnetism 308 (2017) 2123–2128, https://doi.org/10.1140/epjp/s13360-022-02417-z.

[26] M. Janczarek, E. Kowalska, On the origin of enhanced photocatalytic activity of copper-modified titania in the oxidative reaction systems, Catalysts 7 (11) (2017) 317, https://doi.org/10.3390/catal7110317.

[27] J. Montero, L. Österlund, Photodegradation of stearic acid adsorbed on copper oxide heterojunction thin films prepared by magnetron sputtering, Chem. Eng. 2 (3) (2018) 40, https://doi.org/10.3390/chemengineering2030040.

[28] Y. Yue, Enhanced dark adsorption and visible-light-driven photocatalytic properties of narrower-band-gap Cu_2S decorated Cu_2O nanocomposites for efficient removal of organic pollutants, J. Hazard Mater. 384 (2020), 121302, https://doi.org/10.1016/j.jhazmat.2019.121302.

[29] M.K. Kumar, K. Bhavani, G. Naresh, B. Srinivas, A. Venugopal, Plasmonic resonance nature of Ag-Cu/TiO2 photocatalyst under solar and artificial light: synthesis, characterization and evaluation of H2O splitting activity, Appl. Catal. B Environ. 199 (2016) 282–291, https://doi.org/10.1016/j.apcatb.2016.06.050.

[30] M. Tchaplyguine, C.F. Zhang, T. Andersson, O. Bjorneholm, Ag-Cu oxide nanoparticles with high oxidation states: towards new high T-c materials, Dalton Trans. 47 (2018) 16660–16667, https://doi.org/10.1039/C8DT04118K.

[31] Y. Liang, Z. Chen, W. Yao, P.Y. Wang, S.J. Yu, X.K. Wang, Decorating of Ag and CuO on Cu nanoparticles for enhanced high catalytic activity to the degradation of organic pollutants, Langmuir 33 (2017) 7606–7614, https://doi.org/10.1021/acs.langmuir.7b01540.

[32] H.B. Dias, M.I.B. Bernardi, V.S. Marangoni, A.C.A. Bernardi, A.N.S. Rastelli, A. C. Hernandes, Synthesis, characterization and application of Ag doped ZnO nanoparticles in a composite resin, Mater. Sci. Eng., C 96 (2019) 391–401, https://doi.org/10.1016/j.msec.2018.10.063.

[33] M. Jarvin, s. Ashok Kumar, D.R. Rosaline, E.L. Foletto, Remarkable sunlight-driven photocatalytic performance of Ag-doped ZnO nanoparticles prepared by green synthesis for degradation of emerging pollutants in water, Environ. Sci. Pollut. Control Ser. 29 (2022) 1, https://doi.org/10.1007/s11356-022-19796-6.

[34] A.j. Gnanaprakasam, V.M. Sivakumar, M. Thirumarimurugan, A study on Cu and Ag doped ZnO nanoparticles for the photocatalytic degradation of brilliant green dye: synthesis and characterization, Water Sci. Technol. 74 (2016) 6, https://doi.org/10.2166/wst.2016.275.

[35] L. Ye, Xi He, E. Obeng, D. Wang, D. Zheng, T. Shen, J. Shen, R. Hu, H. Deng, Efficiency enhancement of ZnO/Cu_2O solar cells with well oriented and micrometer grain sized Cu_2O films, Appl. Phys. Lett. 112 4 (2018), 042106, https://doi.org/10.1063/1.5017002.

[36] A.M. Mansour, A.M. Fathi, Ali B. Abou Hammad, Amany M El Nahrawy, Microstructures, optical and electrochemical properties of advanced Fe0.8Se0.14Si0.06MoO4 nanocrystalline for energy storage applications, Phys. Scripta 98 5 (2023), 055922, https://doi.org/10.1088/1402-4896/acc9ea.

[37] F. Goumrhar, L. Bahmad, O. Mounkachi, A. Benyoussef, Ab initio calculations of the magnetic properties of TM (Ti, V)-doped zinc-blende ZnO, Int. J. Mod. Phys. B 32 3 (2018), 1850025, https://doi.org/10.1142/S021797921850025x.

[38] K. Yu, H. Ma, Y. Guo, Z. Sun, Y. Dong, I.V. Alexandrov, E.A. Prokofiev, H. Chang, Microstructure evolution and mechanical properties of copper coated graphene

nanoflakes/pure titanium matrix composites, Mater. Char. 194 (2022), 112422, https://doi.org/10.1016/j.matchar.2022.112422.
[39] A.A. Balandin, S. Ghosh, W. Bao, I. Calizo, D. Teweldebrhan, F. Miao, C. Ning Lau, Superior thermal conductivity of single-layer graphene, Nano Lett. 8 3 (2008), 902e907, https://doi.org/10.1021/nl0731872.
[40] Z. Madiha, D. Radouane, D. Bouras, B. Bouzid, R. Barillé, Photocatalytic degradation of orange II by active layers of Ag-doped CuO deposited by spin-coating method, J. Nano Res. Submitted 80 (2023) 1–19.
[41] L. Ye, X. He, E. Obeng, D. Wang, D. Zheng, T. Shen, J. Shen, R. Hu, H. Deng, The CuO and AgO co-modified ZnO nanocomposites for promoting wound healing in Staphylococcus aureus infection Mater, Today Bio 18 (2023), 100552, https://doi.org/10.1016/j.mtbio.2023.100552.
[42] P. Lal Meena, K. Poswal, A.K. r Surela, J.K. Saini, F. synthesis of, ZnO/CuO/Ag2O ternary metal oxide nanocomposite for effective photodegradation of organic water pollutants, 0-20, Water Sci. Technol. 00 (2021), https://doi.org/10.2166/wst.2021.431.
[43] L. Xu, B. Wei, W. Liu, H. Zhang, C. Su, J. Che, Flower-like ZnO-Ag2O composites: precipitation synthesis and photocatalytic activity, Nanoscale Res. Lett. 8 (2013) 536. http://www.nanoscalereslett.com/content/8/1/536.
[44] J. Liu, W. Sun, D. Wei, X. Song, T. Jiao, S. He, W. Zhang, C. Du, Direct growth of graphene nanowalls on the crystalline silicon for solar cells, Appl. Phys. Lett. 106 (2015), 043904, https://doi.org/10.1063/1.4907284.
[45] A.J. Amna Khawer, S. Hussain, Power law, simple symmetry breaking and Hilltop potentials inspired warm inflationary dynamics, Chin. J. Physiol. 59 (2019) 525–534, https://doi.org/10.1016/j.cjph.2019.04.008.
[46] Z. Lu, J. Gao, Q. He, J. Wu, D. Liang, H. Yang, R. Chen, Enhanced antibacterial and wound healing activities of microporous chitosan-Ag/ZnO composite dressing, Carbohydr. Polym. 156 (2017) 460–469, https://doi.org/10.1016/j.carbpol.2016.09.051.
[47] A. Hatamie, A. Khan, M. Golabi, A.P. Turner, V. Beni, W.C. Mak, A. Sadollahkhani, H. Alnoor, B. Zargar, S. Bano, O. Nur, M. Willander, Zinc oxide nanostructure-modified textile and its application to biosensing, photocatalysis, and as antibacterial material, Langmuir 31 (39) (2015) 10913–10921, https://doi.org/10.1021/acs.langmuir.5b02341.
[48] M.I. Khan, K.A. Bhatti, Rabia Qindeel, Norah Alonizan, HayatSaeed Althobaiti, Characterizations of multilayer ZnO thin films deposited by sol-gel spin coating technique, Results Phys. 7 (2017) 651–655, https://doi.org/10.1016/j.rinp.2016.12.029.
[49] M. Ayman Mostafa, E.A. Mwafy, A.M. Khalil, A. Toghan, E.A. Alashkar, ZnO/Ag multilayer for enhancing the catalytic activity against 4-nitrophenol, J. Mater. Sci. Mater. Electron. 34 (2023) 300, https://doi.org/10.1007/s10854-022-09631-6.
[50] B. Allabergenov, U. Shaislamov, H. Shim, M. Jae Lee, A. Matnazarov, B. Choi, Effective control over near band-edge emission in ZnO/CuO multilayered films References and links A comprehensive review of ZnO materials and devices, Opt. Mater. Express 98 1067 (2017) 41301–71101, https://doi.org/10.1364/OME.7.000494, 23479.
[51] H.Q. Shorbagy, M. Alijani, A. Zakeri, E. Heydari, M. Bahonar, M. Slouf, M. Khatami, S. Naderifar, S. Iravani, F.F. Khatami, Dehkordi Green synthesis of bimetallic ZnO-CuO nanoparticles and their cytotoxicity properties, Sci. Rep. 11 (2021) 1, https://doi.org/10.1038/s41598-021-02937-1.
[52] N. Rahimi, V. Dalouji, A. Souri, Studying the optical density, topography, and structural properties of CZO and CAZO thin films at different annealing, Temperatures 6 (2020) 217–223, https://doi.org/10.30501/ACP.2020.107466.
[53] L.C. Chen, C. Hsieh, X. Zhang, Electrical properties of CZO films prepared by ultrasonic spray pyrolysis, Materials 7 (11) (2014) 7304–7313, https://doi.org/10.3390/ma7117304.
[54] R.R. Prabhu, A.C. Saritha, M.R. Shijeesh, M.K. Jayaraj, Fabrication of p-CuO/nZnO heterojunction diode via sol-gel spin coating Technique, Mater. Sci. Eng. B 220 (2017) 82–90, https://doi.org/10.1016/j.mseb.2017.03.008.
[55] P.S. Chen, C.H. Peng, Y.W. Chang, T.W. Lin, S.W. Lee, Improved indium-free transparent ZnO/metal/ZnO electrode through a statistical experimental design method, Mater. Sci. Eng. (2016), https://doi.org/10.1155/2016/7258687.
[56] N. Rahimi, V. Dalouji, Study of the Surface Topography and Optical Properties of ZnO and AZO, CZO, and CAZO Thin Films (In Room Temperature and Annealed at 500 °C), Molecular Crystals and Liquid Crystas, 2022, https://doi.org/10.1080/15421406.2022.2092371.
[57] B. Beatriz, Fonseca, P.L.P. Andrada Silva, A.C. Almeida Silva, N.O. Dantas, A.T. D. Paula, O.C.L. Olivieri, M.E. Beletti, D.A. Rossi, L.R. Goulart, Nanocomposite of Ag-Doped ZnO and AgOnanocrystals as a preventive measure to control biofilm formation in eggshell and salmonella spp. Entry into eggs, Front. Microbiol. 10 (2019) 217, https://doi.org/10.3389/fmicb.2019.00217.
[58] S.H. Kim, A. Umar, S.-W. Hwang, Rose-like CuO nanostructures for highly sensitive glucose chemical sensor application, Ceram. Int. 41 (8) (2015) 9468–9475, https://doi.org/10.1016/j.ceramint.2015.04.003.
[59] Y.N. Rajeswari, A.C. Bose, Absorption–emission study of hydrothermally grown Al: ZnO nanostructures, J. Alloys Compd. 509 (34) (2011) 8493–8500, https://doi.org/10.1016/j.jallcom.2011.06.012.
[60] M. Amalia, C.a D. Ghitulica, M. Popa, R. Mereu, A. Popa, T. PetrisorJr, M. Gabor, A. I. Cadis, B.S. Vasile, Synthesis, structural and morphological characteristics, magnetic and optical properties of Co doped ZnO nanoparticles, Ceram. Int. 40 (2) (2014) 2835–2846, https://doi.org/10.1016/j.ceramint.2013.10.030.
[61] S.S. Alias, A.B. Ismail, A.A. Mohamad, Effect of pH on ZnO nanoparticle properties synthesized by sol–gel centrifugation, J. Alloys Compd. 499 (2) (2010) 231–237, https://doi.org/10.1016/j.jallcom.2010.03.174.
[62] D. Bouras, M. Fellah, A. Mecif, R. Barillé, A. Obrosov, M. Rasheed, High photocatalytic capacity of porous ceramic-based powder doped with MgO, J. Korean Ceram. Soc. 60 (2023) 155–168, https://doi.org/10.1007/s43207-022-00254-5.
[63] D. Bouras, M. Rasheed, R. Barille, Mustafa Nuhad Aldaraji, Efficiency of adding DD3+(Li/Mg) composite to plants and their fibers during the process of filtering solutions of toxic organic dyes, Opt. Mater. 131 (2022), 112725, https://doi.org/10.1016/j.optmat.2022.112725.
[64] S. Hemant, G. Chauhan, A.K. Jain, S.K. Sharma, Adsorptive potential of agricultural wastes for removal of dyes from aqueous solutions, J. Environ. Chem. Eng. 5 1 (2017) 122–135.
[65] D. Bouras, A. Mecif, R. Barillé, A. Harabi, M. Rasheed, A. Mahdjoub, M. Zaabat, Cu: ZnO deposited on porous ceramic substrates by a simple thermal method for photocatalytic application, Ceram. Int. 44 (17) (2018) 21546–21555, https://doi.org/10.1016/j.ceramint.2018.08.218.
[66] B. Dikra, A. Mecif, A. Harabi, R. Barillé, A.H. Mahdjoub, MouradZaabat, economic and ultrafast photocatalytic degradation of orange II using ceramic powders, Catalysts 11 6 (2021) 733, https://doi.org/10.3390/catal11060733.
[67] X. Yu, H.N. Tsao, Z. Zhang, P. Gao, Miscellaneous and perspicacious: hybrid halide perovskite materials based photodetectors and sensors, J. Adv. Opt. Mater. (2020), 2001095, https://doi.org/10.1002/adom.202001095.
[68] S. Safa, S. Mokhtari, A. Khayatian, R. Azimirad, Improving ultraviolet photodetection of ZnOnanorods by Cr doped ZnO encapsulation process, Opt Commun. 413 (2018) 131–135, https://doi.org/10.1016/j.optcom.2017.12.038.
[69] V.S. Bhati, S. Ranwa, M. Fanetti, M. Valant, M. Kumar, Efficient hydrogen sensor based on Ni-doped ZnO nanostructures by RF sputtering, Sens. Actuators, B 255 (2018) 588–597, https://doi.org/10.1016/j.snb.2017.08.106.
[70] L.X. Qian, Y. Wang, Z.H. Wu, T. Sheng, X.Z. Liu, β-Ga_2O_3 solar-blind deep-ultraviolet photodetector based on annealed sapphire substrate 140 (2017) 106–110.
[71] F. Abbasi, F. Zahedi, M.h. Yousef, Performance Improvement of UV Photodetectorsusing Cd-Doped ZnO Nanostructures, 2021, https://doi.org/10.21203/rs.3.rs-328527/v1. Research Article.
[72] V.S. Bhati, S. Ranwa, M. Fanetti, M. Valant, M. Kumar, Efficient hydrogen sensor based on Ni-doped ZnO nanostructures by RF sputtering, Sensor. Actuator. B Chem. 255 (2018) 588–597, https://doi.org/10.1016/j.snb.2017.08.106.
[73] Z.M. Zhang, Y. Ning, X.S. Fang, From nanofibers to ordered ZnO/NiO heterojunction arrays for self-powered and transparent UV photodetectors, J. Mater. Chem. C 7 (2019) 223–229, https://doi.org/10.1039/C8TC05877F.
[74] L. Zhang, Y. Wang, H. Wu, M. Hou, J. Wang, L. Zhang, C. Liao, S. Liu, Y. Wang, A ZnO nanowire-based microfiber coupler for all-optical photodetection, Appl. Nano. 11 (2019) 8319–8326, https://doi.org/10.1039/C9NR02040C.
[75] M. Zheng, P. Gui, X. Wang, G. Zhang, J. Wan, H. Zhang, G. Fang, H. Wu, Q. Lin, C. Liu, ZnO ultraviolet photodetectors with an extremely high detectivity and short response time, Appl. Surf. Sci. 481 (2019) 437–442, https://doi.org/10.1016/j.apsusc.2019.03.110.
[76] N. Hezil, M. Fellah, Synthesis, structural and mechanical properties of nanobioceramic (α-Al_2O_3), 2019, J. Aust. Ceram. Soc. 55 (2019) 1167–1175.